Long-range structural defects by pathogenic mutations in most severe glucose-6-phosphate dehydrogenase deficiency

Naoki Horikoshi[a,b,c], Sunhee Hwang[d], Cornelius Gati[b,c], Tsutomu Matsui[e], Carlos Castillo-Orellana[f], Andrew G. Raub[d], Adriana A. Garcia[d], Fatemeh Jabbarpour[b,c], Alexander Batyuk[g], Joshua Broweleit[c], Xinyu Xiang[c], Andrew Chiang[c], Rachel Broweleit[c], Esteban Vöhringer-Martinez[f], Daria Mochly-Rosen[d,1], and Soichi Wakatsuki[b,c,1]

[a]Life Science Center for Survival Dynamics, University of Tsukuba, Ibaraki 305-8577, Japan; [b]Biological Sciences Division, SLAC National Accelerator Laboratory, Menlo Park, CA 94025; [c]Department of Structural Biology, Stanford University School of Medicine, Stanford, CA 94305; [d]Department of Chemical and Systems Biology, Stanford University School of Medicine, Stanford, CA 94305; [e]Stanford Synchrotron Radiation Lightsource, SLAC National Accelerator Laboratory, Menlo Park, CA 94025; [f]Departamento de Físico-Química, Facultad de Ciencias Químicas, Universidad de Concepción, Concepción 94030000, Chile; and [g]Linac Coherent Light Source, SLAC National Accelerator Laboratory, Menlo Park, CA 94025

Edited by Anton Berns, Netherlands Cancer Institute, Amsterdam, Netherlands, and approved December 17, 2020 (received for review November 10, 2020)

Glucose-6-phosphate dehydrogenase (G6PD) deficiency is the most common blood disorder, presenting multiple symptoms, including hemolytic anemia. It affects 400 million people worldwide, with more than 160 single mutations reported in G6PD. The most severe mutations (about 70) are classified as class I, leading to more than 90% loss of activity of the wild-type G6PD. The crystal structure of G6PD reveals these mutations are located away from the active site, concentrating around the noncatalytic $NADP^+$-binding site and the dimer interface. However, the molecular mechanisms of class I mutant dysfunction have remained elusive, hindering the development of efficient therapies. To resolve this, we performed integral structural characterization of five G6PD mutants, including four class I mutants, associated with the noncatalytic $NADP^+$ and dimerization, using crystallography, small-angle X-ray scattering (SAXS), cryogenic electron microscopy (cryo-EM), and biophysical analyses. Comparisons with the structure and properties of the wild-type enzyme, together with molecular dynamics simulations, bring forward a universal mechanism for this severe G6PD deficiency due to the class I mutations. We highlight the role of the noncatalytic $NADP^+$-binding site that is crucial for stabilization and ordering two β-strands in the dimer interface, which together communicate these distant structural aberrations to the active site through a network of additional interactions. This understanding elucidates potential paths for drug development targeting G6PD deficiency.

G6PD deficiency | structural defects | $NADP^+$ | hemolytic anemia | enzymopathy

Glucose-6-phosphate dehydrogenase (G6PD) deficiency is one of the most prevalent human disorders, resulting in hemolytic anemia, neonatal jaundice, and kernicterus (1–4). More than 400 million people have mutations in the G6PD gene, and more than 70 mutants are known to cause severe symptoms (5). G6PD is a rate-limiting enzyme in the pentose phosphate pathway (PPP). PPP is essential for nucleotide synthesis and biosynthesis of fatty acids, cholesterol, steroid hormones, and catecholamines by consuming NADPH (6). G6PD transfers protons and electrons from glucose-6-phosphate (G6P) to $NADP^+$ to produce NADPH, which is critical for reducing reactive oxygen species (ROS) by producing a reduced form of glutathione (7). Thus, the enzymatic activity of G6PD is essential for reducing ROS. In particular, G6PD is the key enzyme that can produce NADPH in red blood cells (RBCs), which lack mitochondria and other sources of NADPH. Therefore, the loss of the G6PD activity in RBCs causes acute hemolysis under the oxidative stress, induced by infection, by some medications, and by foods such as fava beans (8, 9). In the coding region of the G6PD gene, more than 160 single missense mutations have been reported, and the World Health Organization (WHO) classified them into five classes depending on the levels of their enzyme activity and the resulting symptoms in the carriers (1, 10–13). Class I pathogenic mutations are the most severe type, in which mutated enzymes show less than 10% activity compared to the wild type and is symptomized by congenital nonspherocytic hemolytic anemia (10).

Human G6PD comprises 515 amino acids and has two $NADP^+$-binding sites and one G6P-binding site (14, 15). One of the two $NADP^+$-binding sites right next to the G6P-binding site is called catalytic, while the other site, remote from G6P, is called structural (noncatalytic). G6PD molecules form a homodimer and/or a homotetramer as a functional unit, whereas the monomeric form is inactive (16–20). Previously, the structure of the class II Canton mutant (R459L), whose mutation is located close to the catalytic site, was reported (14, 21). The structure of the Canton mutant showed that the overall structure is very similar to that of the wild-type G6PD, but the molecular mechanisms of the loss of activity of the G6PD pathogenic mutants have been unclear (14, 15). More recently, we have identified an

Significance

Mechanism of the loss of activity of the most severe patient-derived mutants of glucose-6-phosphate dehydrogenase (G6PD) deficiency has remained elusive despite the availability of the G6PD structures for decades. Structural and biophysical investigations have revealed a common mechanism and dynamics of how these mutations hinder the substrate-binding site, reducing enzymatic activity. These are triggered by a long-distance propagation of structural defects at the dimer interface and the binding site of the noncatalytic cofactor. These structural distortions are found among all of the class I mutants investigated, providing critical clues for drug design to address G6PD deficiency by correcting the structural defects.

Author contributions: N.H., D.M.-R., and S.W. designed research; N.H., S.H., C.G., T.M., C.C.-O., A.G.R., A.A.G., F.J., J.B., X.X., A.C., R.B., and E.V.-M. performed research; N.H., S.H., C.G., T.M., A.B., and E.V.-M. analyzed data; and N.H., S.H., T.M., A.A.G., E.V.-M., D.M.-R., and S.W. wrote the paper.

The authors declare no competing interest.

This article is a PNAS Direct Submission.

[1]To whom correspondence may be addressed. Email: mochly@stanford.edu or soichi.wakatsuki@stanford.edu.

This article contains supporting information online at https://www.pnas.org/lookup/suppl/doi:10.1073/pnas.2022790118/-/DCSupplemental.

Published January 18, 2021.

activator compound, AG1, that greatly increases the catalytic activities of the Canton and other pathogenic class II and class III mutants, by stabilizing the dimeric states (21, 22); AG1 bridges the monomer/monomer interface close to the structural $NADP^+$-binding sites of two interacting G6PD monomers. Interestingly, many class I mutations are not activated by AG1, although these mutations are often located in and around the structural $NADP^+$ site and the dimer interface, both distant from the catalytic site (1, 13) (*SI Appendix*, Fig. S1). The structural $NADP^+$ has been known to stabilize the G6PD dimer form and maintain the enzymatic activity (14, 18–26). However, the molecular mechanisms of the loss of activity and instability of G6PD by the class I pathogenic mutations located around the structural $NADP^+$ and dimer interface have been elusive, severely limiting the development of efficient therapy for class I mutations. In this study, we determined the structures of the class I pathogenic mutants of G6PD deficiency by X-ray crystallography, small-angle X-ray scattering (SAXS), and cryogenic electron microscopy (cryo-EM) complemented with molecular dynamics (MD) simulations and biophysical analyses to elucidate the molecular mechanisms of dysfunction of the catalytic activity in G6PD deficiency.

Results

Structure of the Pathogenic Mutant, G6PD P396L, Revealed a Distortion in the Dimer and Loss of the Structural $NADP^+$ Binding. To uncover the molecular mechanisms leading to the loss of G6PD's function in class I mutants, we focused on proline 396, a residue located at the structural $NADP^+$-binding site that is mutated to arginine or leucine in two class I mutations (27, 28). We used size exclusion chromatography (SEC) to probe protein oligomerization and found wild-type G6PD ($G6PD^{WT}$) oligomerization was concentration dependent; $G6PD^{WT}$ formed a tetramer at a higher concentration and shifted to a dimer/monomer at a lower concentration. In contrast, the G6PD P396L mutant ($G6PD^{P396L}$) did not form a tetramer at higher concentrations (*SI Appendix*, Fig. S2), suggesting point mutations at the structural $NADP^+$-binding site disrupt the quaternary structure of G6PD.

To understand how mutations at the structural $NADP^+$ site disrupted G6PD quaternary structure and protein function, we solved the crystal structure of $G6PD^{P396L}$ at 3.07-Å resolution (Fig. 1*A* and *SI Appendix*, Table S1), revealing distinct structural differences. First, $G6PD^{P396L}$ formed a dimer while $G6PD^{WT}$ formed a tetramer in the crystal. Second, major structural changes were observed between the $G6PD^{P396L}$ and $G6PD^{WT}$ dimers (Fig. 1 *B–D*); when the top monomers of $G6PD^{WT}$ (dark blue) and $G6PD^{P396L}$ (dark green) were superimposed (Fig. 1 *D*, *Top*), the distance between the Cα-carbon atoms of Glu93 residues of the bottom monomers in the $G6PD^{WT}$ (light blue) and the $G6PD^{P396L}$ (light green) dimers was 29 Å (Fig. 1 *D*, *Bottom*), indicating a large distortion of the overall dimer structure. Additionally, electron density was missing for the C-terminal tail, two β-strands (βM and βN) at the dimer interface, and the structural $NADP^+$ in the $G6PD^{P396L}$ structure, although the catalytic $NADP^+$ was present (Fig. 1*A*). This contrasts with the reported $G6PD^{WT}$ structures; the structural $NADP^+$ is often observed in the absence of $NADP^+$ supplementation, and the catalytic $NADP^+$ is only observed when $NADP^+$ is supplemented (15, 21). The presence of structural $NADP^+$ in the $G6PD^{WT}$ crystal structure is consistent with kinetic studies showing the structural $NADP^+$ bound with two orders of magnitude higher affinity than the catalytic $NADP^+$ (19).

Since structural $NADP^+$ is known to stabilize G6PD, we measured protein stabilities of $G6PD^{WT}$ and $G6PD^{P396L}$ using a thermal shift assay. Consistent with the absence of structural $NADP^+$ in the $G6PD^{P396L}$ structure, the thermal shift assay revealed that $G6PD^{P396L}$ is less stable than $G6PD^{WT}$ and $NADP^+$ had only a small effect on $G6PD^{P396L}$ (Fig. 1*E*). In contrast, $NADP^+$ significantly stabilized $G6PD^{WT}$ by more than 10 °C (Fig. 1*F*); $NADP^+$-dependent stabilization of $G6PD^{WT}$ is likely due to the structural $NADP^+$-binding site and dimer stabilization. This suggests the structural $NADP^+$ binding to $G6PD^{P396L}$ is impaired, consistent with the crystal structure of $G6PD^{P396L}$.

To ensure crystal packing did not influence structural observations, we employed cryo-EM single particle structural analysis, which is free from crystal contacts. The crystal structure of the $G6PD^{P396L}$ dimer superimposed well with the cryo-EM map of the $G6PD^{P396L}$ (Fig. 1*G* and *SI Appendix*, Fig. S3). Further cryo-EM analysis of the $G6PD^{P396L}$ structure revealed that the dimer interface was less well defined than the core domains (Fig. 1*G*). In addition, the cryo-EM map of $G6PD^{WT}$ superimposed well with the crystal structure of the $G6PD^{WT}$ tetramer, and the density of the dimer interface was solid (Fig. 1*H*), in stark contrast with that of $G6PD^{P396L}$ (Fig. 1*G*). Taken together, the structural and biophysical analyses of the $G6PD^{P396L}$ showed that the class I single point mutation P396L caused the loss of the structural $NADP^+$ binding and drastic structural changes in the overall dimer structure. Additionally, distortion of the dimer structure disrupts the dimer–dimer interface, which may explain why $G6PD^{P396L}$ does not form a tetramer in the SEC analysis.

Structures of the G6PD P396L Mutant in Solution. To determine whether structural differences observed in crystals could be captured in solution, we studied the solution structures of $G6PD^{P396L}$ and $G6PD^{WT}$ using small-angle X-ray scattering coupled with size exclusion chromatography (SEC-SAXS). To obtain discrete dimer and tetramer fractions of $G6PD^{WT}$, SEC-SAXS measurements were performed with or without G6P. As expected, the $G6PD^{WT}$ tetramer dissociated into a dimer in the presence of G6P (*SI Appendix*, Fig. S2*E*). Guinier and $P(r)$ analyses showed similar R_g and D_{max} values between $G6PD^{P396L}$ and $G6PD^{WT}$ (*SI Appendix*, Fig. S4 and Table S2). The estimated Porod volumes indicated that both $G6PD^{P396L}$ and $G6PD^{WT}$ with G6P were primarily in the dimer form in solution. In contrast, the experimental scattering data exhibited slightly different profiles in the middle-angle region (approximately $q = 0.05$ to 0.15 $Å^{-1}$), which was more pronounced in the Kratky plot (Fig. 2*A*). These observations suggested that $G6PD^{P396L}$ had a different conformation from that of $G6PD^{WT}$ in solution (29).

Since the $G6PD^{P396L}$ crystal structure lacked disordered regions (βM and βN strands and the C-terminal tails), we performed SAXS modeling using the program *CORAL* to reconstruct the disordered regions (30). We ran 20 repetitions of modeling with the coordinates of A399-T423 (βM to βN) as a rigid structure and M1-H27, V394-E398, Y424-D435, and the C-terminal tail as flexible loops. Note that all the other structural components visible in the crystal were fixed during the modeling (*Materials and Methods*). The calculated SAXS profiles of the initial and resulting *CORAL* model were well superimposed to the experimental scattering profile (Fig. 2*B* and *SI Appendix*, Fig. S4*U*). Due to the lack of the N-terminal tail (M1-H27) in the crystal structure of $G6PD^{WT}$, an additional *CORAL* modeling was employed for complementing the N-terminal tail. The calculated scattering profile fit well to the experimental scattering profile of $G6PD^{WT}$ (Fig. 2*C*), clearly demonstrating that the crystal structure was conserved in solution. In addition, the calculated scattering profile using the crystal structure of the $G6PD^{WT}$ tetramer with the added model of the N-terminal tail also fit well to the experimental SAXS profile of the tetramer fraction of $G6PD^{WT}$ (Fig. 2*D*). These SAXS results corroborate that the significant structural changes of $G6PD^{P396L}$ observed in the crystal structure are indicative of structures in solution and are the cause for the loss of activity of the mutant enzymes.

Loss of the Structural $NADP^+$ Caused a Partial Deformation of the β-Sheet. To understand how structural defects in the $G6PD^{P396L}$ dimer conformation result in the loss of the enzyme function, we investigated the $G6PD^{P396L}$ dimer structure in further detail. Structural

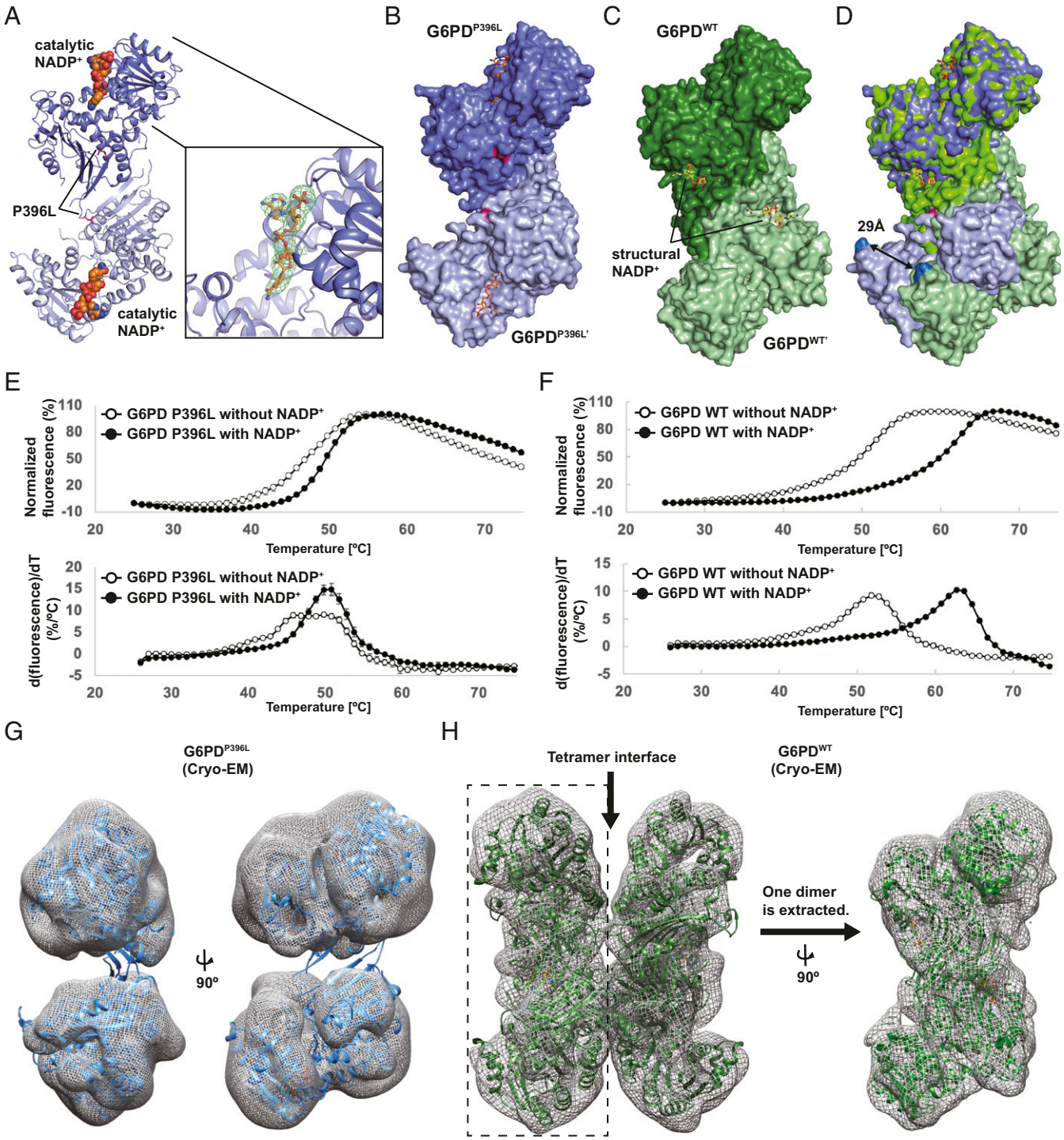

Fig. 1. Overall structure of the class I mutant, G6PD^{P396L}. (*A*) Overall structure of the dimer G6PD^{P396L}. Two G6PD molecules and the catalytic NADP$^+$ are shown in blue, light blue, and orange, respectively. The catalytic NADP$^+$-binding site is shown in close-up view on the *Right*. The Fo-DFc map for the catalytic NADP$^+$ is contoured at 3.0σ level. (*B*) Space filling model of the dimer G6PD^{P396L}. (*C*) Space filling model of the dimer G6PD^{WT}. (*D*) Superimposition of the dimer G6PD^{P396L} and G6PD^{WT}. Distance between Cα-carbon atoms of E93 residues in the G6PD^{P396L} and G6PD^{WT} structures are shown. (*E* and *F*) The thermal denaturation curves of the G6PD^{P396L} and G6PD^{WT} with or without NADP$^+$ (*Top*). The error bars indicate the SDs ($n = 4$). *Bottom* shows the derivative values of the thermal denaturation curves on the *Top*. (*G*) Crystal structure of G6PD^{P396L} dimer is superimposed with the cryo-EM map of G6PD^{P396L}. The G6PD^{P396L} dimer on the *Left* is rotated by 90° on the *Right*. (*H*) Crystal structure of the G6PD^{WT} tetramer (PDB ID: 6E08) is superimposed with the cryo-EM map of G6PD^{WT}. The cryo-EM map of the *Left* half on the *Left* (enclosed with a dashed rectangle) is extracted and rotated by 90°. The crystal structure of the G6PD^{WT} dimer (PDB ID: 6E08) is superimposed with the cryo-EM map on the *Right*.

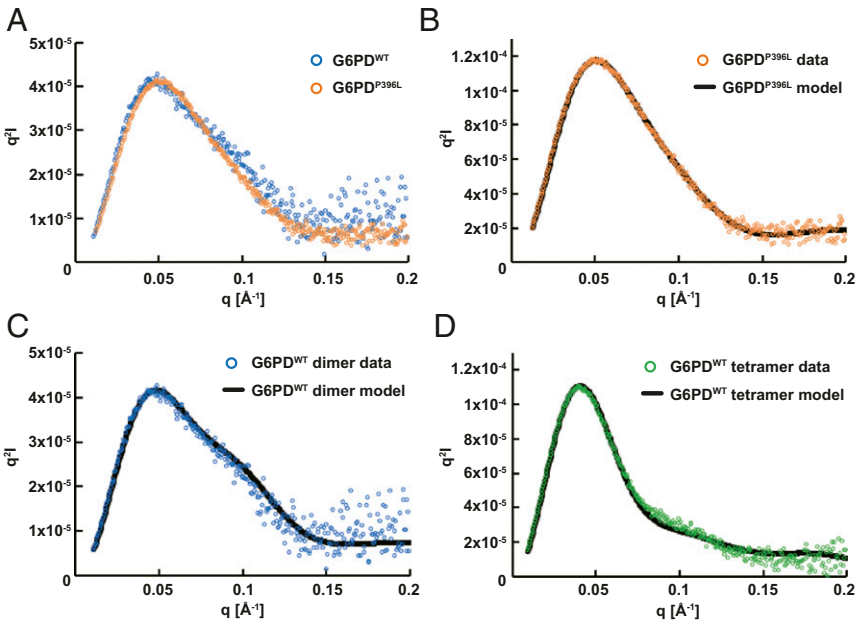

Fig. 2. Structural analysis of the G6PD^{P396L} in solution. SEC-SAXS experiments were performed to study the G6PD^{WT} dimer (blue), G6PD^{P396L} (orange), and G6PD^{WT} tetramer (green). (*A*) Kratky plots of G6PD^{WT} dimer and G6PD^{P396L}. The plot of G6PD^{P396L} is scaled to that of G6PD^{WT} dimer. Curvatures in the middle q region are significantly different. (*B–D*) The program *CORAL* was employed for SAXS modeling. The theoretical Kratky plot of the best *CORAL* model is fitted with the experimental data.

analysis of G6PD^{P396L} revealed two β-strands (βM and βN) after the P396L residue were disordered, suggesting proline 396 may bend the adjacent loop to allow antiparallel β-sheet formation between βL and βM (Fig. 3 *A* and *B*). Additionally, we observed disorder in the C-terminal tail and the loss of the structural NADP$^+$ binding (Figs. 1*A* and 3*B*). This suggests that the β-sheet and the C-terminal tail cooperatively sandwich the structural NADP$^+$ between them, which is consistent with the high affinity of the structural NADP$^+$ in G6PD^{WT} (19).

To understand the role of the structural NADP$^+$ in maintaining the stable dimer interface, we carried out MD simulations of G6PD^{WT} [Protein Data Bank (PDB) ID: 6E08] with and without NADP$^+$ molecules bound at the structural NADP$^+$-binding sites in aqueous solution. To create an apo form structure for MD simulations, we eliminated the structural NADP$^+$ from the crystal structure coordinates. The MD simulations of G6PD^{WT} with the structural NADP$^+$ showed that the protein tetramer maintained its initial conformation, including the close interaction of the C-terminal tail with the structural NADP$^+$. In contrast, in the apo form, the C-terminal tail was completely disordered (Movie S1), which is consistent with the X-ray structure of the G6PD^{P396L} mutant without NADP$^+$ and the SAXS modeling results. Because G6PD^{P396L} was shown to be dimeric in both solution and crystals, we also simulated the apo and the structural NADP$^+$-bound dimers. Fig. 3*C* shows a representative snapshot confirming the disorder of the C-terminal tail (*SI Appendix*, Fig. S5 and Movies S2 and S3), displaying significant root mean square deviations (rmsd) of the Cα-carbon atom positions at the C-terminal tail of the apo compared to the holo form in six independent simulations.

Interestingly, the βN strand and the loop adjacent to βN located at the dimer interface deformed, opening a wedge between the last two β-strands βM and βN (Fig. 3*C*). All six independent simulations of the apo form showed the loss of the secondary structures in these strands in one of the two monomers during the 1-μs trajectories (*Materials and Methods*). In all the simulations of the NADP$^+$ bound dimer (holo form), in contrast, the strands βM and βN maintained their conformation. These results could indeed represent the beginning of the loss of the last two β-strands observed in the G6PD^{P396L} mutant. The deformation of the βN strand occurred on both monomers at different times in the MD trajectories, suggesting vulnerability of the dimer interface in the absence of the two structural NADP$^+$ molecules. The trajectory length of up to 1 μs was not long enough to observe the complete unfolding of the dimer interface observed in the mutant X-ray and cryo-EM structures. However, the MD simulations provided additional evidence that the loss of the structural NADP$^+$ due to the mutations unlocked the C-terminal tail of both monomers and triggered the unzipping of the βM and βN strands.

Next, we addressed the effect of the G6PD^{P396L} mutation on the stability of the structural NADP$^+$. Our previous results indicated that the first step was the loss of the sandwich-like conformation of the C-terminal tail on top of NADP$^+$. To account for this first event required for a possible binding/unbinding process, we created a C-terminal tail-truncated variant of the wild-type and G6PD^{P396L} dimer in silico with NADP$^+$ bound to both monomers in the structural site. Six independent simulations of 500 ns showed that the mutation led to larger root mean square fluctuations of atoms in the nicotinamide and ribose groups of NADP$^+$ compared to the wild-type enzyme. Furthermore, the simulations showed some partial unbinding events of NADP$^+$'s nicotinamide end together with the unzipping between the βM and βN strands (*SI Appendix*, Fig. S6 and Movie S4). These results provide further evidence that the P396L mutation destabilizes the structural NADP$^+$-binding site.

In summary, the MD simulations revealed that the absence of NADP$^+$ in the structural site was responsible for increasing the C-terminal tail's flexibility and destabilizing the βN strand. These data are consistent with the mutant crystal structures, SAXS, and cryo-EM results. Furthermore, the P396L mutation destabilized the NADP$^+$-binding site interactions, thus inducing increased fluctuation of NADP$^+$'s nicotinamide end with sporadic unbinding events in the in silico-created C-terminal tail-truncated G6PD dimer compared to the wild type.

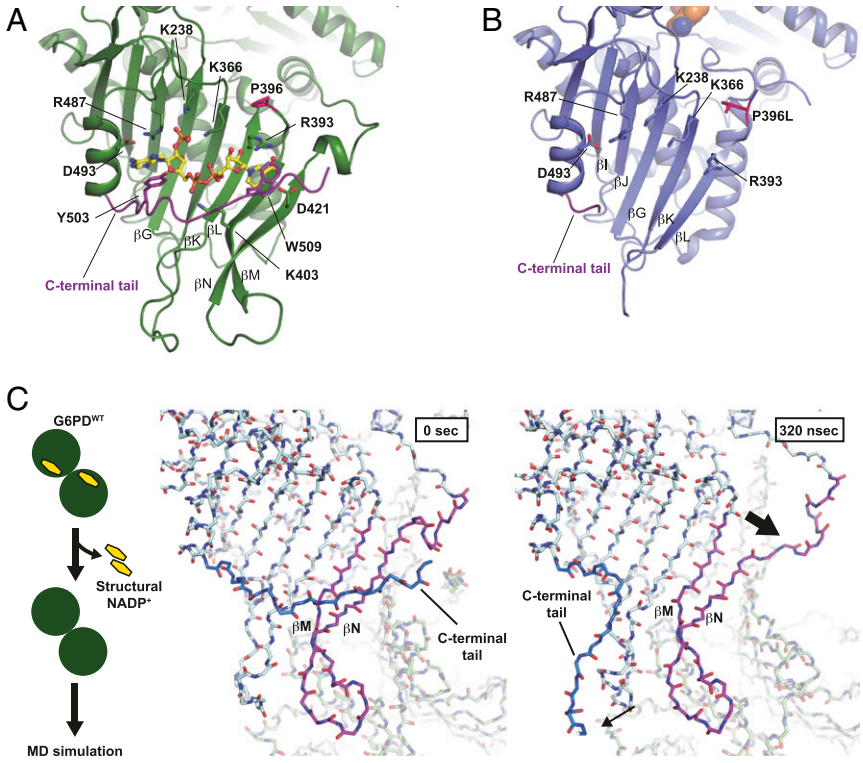

Fig. 3. Loss of the structural NADP+ caused a partial deformation of the β-sheet. (*A*) Close-up view of the structural NADP+-binding site in G6PD^{WT}. G6PD^{WT} molecule is shown in green. Residues responsible for the structural NADP+ binding are shown. C-terminal tail is shown in purple. Structural NADP+ is shown in yellow. (*B*) Close-up view of the structural NADP+-binding site in G6PD^{P396L}. A G6PD^{P396L} monomer is shown in blue. Residues responsible for the structural NADP+ binding in G6PD^{WT} are shown. (*C*) MD simulation of the structure of G6PD^{WT} (PDB ID: 6E08). Scheme of the MD simulation is shown at *Left*. Snapshots of the G6PD dimer without the structural NADP+ at 0 (*Middle*) and 320 ns (*Right*), respectively.

Long Distance Communication between the Structural NADP+ Site and the G6P-Binding Site. In addition to the partial deformation of the β-sheet, the disorder of βM and βN strands in G6PD^{P396L} changed the interaction between the βL-βM strands and αf helix (β–α interaction) (Fig. 4 *A* and *B*). In the G6PD^{WT} structure, I392, V394, and V400 residues of the β-strands hydrophobically interacted with M207, L211, and L214 residues of the αf helix (Fig. 4*A*). In contrast, the β–α interaction in G6PD^{P396L} seemed to be weakened (Fig. 4*B*). In addition, the βM and βN strands and the loop between βK and βL in one of the two monomers of the G6PD dimer, which were disordered in the G6PD^{P396L} mutant, were essential for the interaction with the αf helix in the other G6PD monomer of the G6PD dimer (Fig. 4 *C* and *D*). In particular, the F381 residue, at which the substitution to leucine is a class I mutation, hydrophobically interacted with M212, V213, F216, and A217 residues. In addition, the K407 residue, whose substitution to threonine is a class II mutation, electrostatically interacted with E206 (31–33) (Fig. 4*C*). Destabilization of the αf helix in G6PD^{P396L} rendered the αf helix shifted toward the G6P-binding site by one helical turn, and as a result, the stretched αf´ helix occluded the G6P-binding site (Fig. 4 *E* and *F*). H201, Y202, and K205 residues are responsible for the interaction with G6P in the wild-type G6PD (15) (Fig. 4*E*). In contrast, H201 and Y202 in G6PD^{P396L} formed a π-stacking with the nicotinamide ring of the catalytic NADP+, which might stabilize the inactive state of the pathogenic mutants (Fig. 4*F* and *SI Appendix*, Fig. S7 *A* and *B*). Consistent with this observation, the isothermal titration calorimetry experiment with G6PD^{WT} and G6PD^{P396L} revealed that G6P was bound to G6PD^{WT}, but not to G6PD^{P396L} (Fig. 4 *G* and *H*). The SEC analysis of G6PD^{WT} and G6PD^{P396L} with or without G6P supported the notion that G6PD^{P396L} was not responsive to G6P (*SI Appendix*, Fig. S2 *E* and *F*). Together, the stable interactions between the αf helix and the βL-βM strands as well as the loop between βK and βL were essential for the formation and proper placement of the αf and αf´ helices for G6P recognition and binding, and thus supporting the catalytic activity.

Universal Mechanism of Inactivation of the Pathogenic Type I Mutants by Loss of the Structural NADP+. The structural changes in G6PD^{P396L} were caused by disruption of long-range communication among the C-terminal tail, structural NADP+, β-sheet (βG to βN), and αf helix. Based on these observations, we hypothesized that the multifaceted structural changes in G6PD^{P396L} might occur in other class I pathogenic mutants, which affected the structural NADP+ binding, β–α interaction, and dimerization. R393 directly interacts with the structural NADP+, and R393H and R393G mutations have been reported as class I mutations in North America and Italy (31, 34, 35) (Fig. 3*A*). As mentioned above, F381, I392, and V394 help hold the αf and αf´ helices at the proper position in the wild-type G6PD. Consistent with that, F381L, I392T, and V394L mutations are classified as class I pathogenic mutations in patients from Poland, Finland, Sweden, and the Czech Republic (33, 36). To address our hypothesis on a common structural defect among class I G6PD mutations, we determined the structures of three additional class I mutants. These were: G6PD V394L (G6PD^{V394L}), in which V394 is mutated to leucine in the β–α interaction site; G6PD F381L (G6PD^{F381L}), in which F381 is mutated to leucine in the dimer interface; and G6PD R393H (G6PD^{R393H}), in which R393 is mutated to histidine in the structural NADP+-binding site. The structures of G6PD^{F381L}, G6PD^{V394L}, and G6PD^{R393H} revealed that the C-terminal tail, structural NADP+, βM-βN strands were disordered, followed by αf helix shifting to the G6P-binding site, similar to the structure

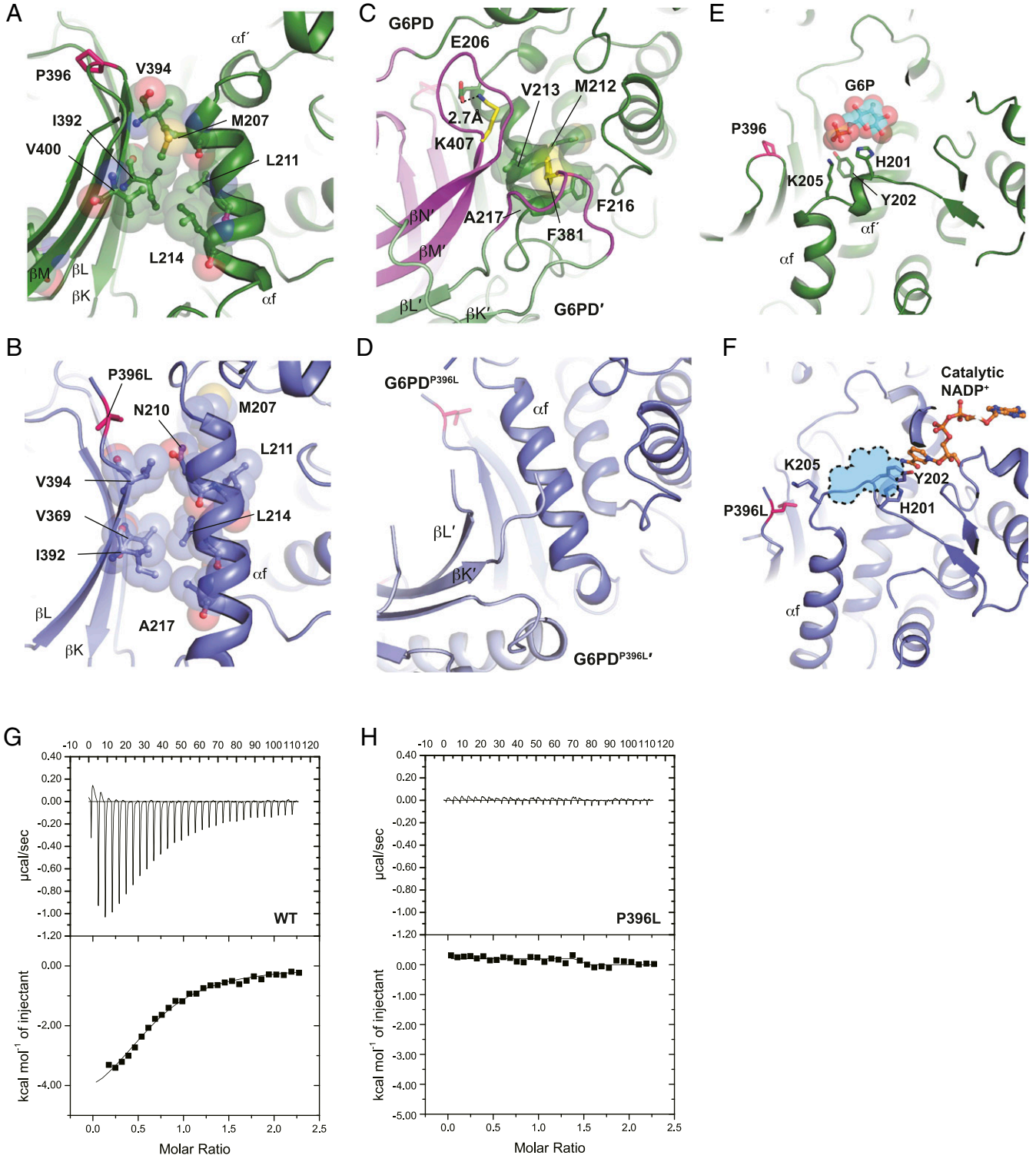

Fig. 4. Loss of the structural $NADP^+$ causes the structural change in the G6P-binding site. (*A*) Close-up view of the interface between the β-sheet and αf helix in $G6PD^{WT}$. (*B*) Close-up view of the interface between the β-sheet and αf helix in $G6PD^{P396L}$. (*C*) Dimer interface in the $G6PD^{WT}$ structure. Two $G6PD^{WT}$ molecules are shown in green and light green, respectively. Disordered regions in $G6PD^{P396L}$ are colored in magenta. F381 and K407 residues are shown in yellow. (*D*) Dimer interface in the $G6PD^{P396L}$ structure. Two $G6PD^{P396L}$ molecules are shown in blue and light blue, respectively. (*E*) Close-up view of the G6P-binding site in $G6PD^{WT}$ (PDB ID: 2BHL) (15). A G6P molecule is shown in cyan. Phosphorus and oxygen atoms are shown in orange and red, respectively. (*F*) Close-up view of the G6P-binding site in $G6PD^{P396L}$. Catalytic $NADP^+$ is shown in orange. G6P-binding site in $G6PD^{WT}$ is shown in sky blue. (*G*) The isothermal titration calorimetry analysis of $G6PD^{WT}$ with G6P. (*H*) The isothermal titration calorimetry analysis of $G6PD^{P396L}$ with G6P.

of G6PD^{P396L} (*SI Appendix*, Fig. S8 and Table. S3). In addition, G6PD^{F381L}, G6PD^{V394L}, and G6PD^{R393H} were hardly responsive to G6P and NADP$^+$ (*SI Appendix*, Fig. S9), suggesting that the structural NADP$^+$ and G6P had difficulty accessing those binding sites. Taken together, the structures of several class I pathogenic mutants of G6PD identified defects associated with the structural NADP$^+$ and dimerization as a common mechanism of the loss of enzyme activity in this enzymopathy.

Structure-Based Mutagenesis Further Validates the Role of the Structural NADP$^+$. According to our structures of the class I mutants, the cooperative interaction of the C-terminal tail and the structural NADP$^+$ is essential to maintain the proper antiparallel β-sheet (βG and βI to βN) (Fig. 3 *A* and *B*) as part of the continuous 18-strand β-sheet in the dimer (nine strands/monomer). Consistent with this idea, an alanine mutation of W509 (G6PD^{W509A}) in the C-terminal tail, which disrupts the π-stacking between the indole ring of W509 and nicotinamide ring of the structural NADP$^+$, showed the same structural features with the other class I mutants (*SI Appendix*, Fig. S10 *A–C*). The G6PD^{W509A} mutant also showed no response to G6P in the SEC analysis (*SI Appendix*, Fig. S10*D*). The G6PD^{W509A} mutant had ∼30% activity and a similar K_m value compared to G6PD^{WT}, even though the structure of G6PD^{W509A} suggested that the enzyme is in an inactive state (*SI Appendix*, Table S4 and *Supplementary Methods*). We found that the B factors of the Cα atoms of the residues responsible for G6P binding in G6PD^{WT} were quite low compared to the baseline, whereas those in G6PD^{W509A} and the other class I mutants were slightly higher (*SI Appendix*, Fig. S10*E*), suggesting that a structural transition between the inactive and active states may occur. Consistent with this idea, the thermal shift assay with or without NADP$^+$ revealed that G6PD^{W509A} was responsive to NADP$^+$ but less stable than G6PD^{WT} (*SI Appendix*, Fig. S10*F*).

Discussion

The structural NADP$^+$ in G6PD has been thought to maintain the catalytic activity by stabilizing its dimer conformation. However, the molecular mechanisms underlying dysfunction of G6PD associated with the loss of the structural NADP$^+$, as well as the role of dimerization for catalysis, have not been elucidated at the atomic and molecular levels. To investigate the molecular mechanisms of the loss of enzymatic activity and stability, we also determined the structures of the other class I pathogenic mutants of G6PD deficiency, P396L, V394L, F381L, and R393H.

The SEC-SAXS analysis and *CORAL* modeling of G6PD^{P396L} suggested that the disordered βM and βN strands might be settled in the cavity, close to the catalytic site (*SI Appendix*, Fig. S4 *S* and *T*). In addition, the proper conformation of the β-sheet was essential to hold the αf helix at the appropriate position. Disruption of these structural features made the αf′ helix unwound and occupied the G6P-binding site (Figs. 4 *E* and *F* and 5). These lines of structural evidence are consistent with our biophysical analysis results, which showed that the pathogenic G6PD class I mutants were less responsive to G6P and the structural NADP$^+$, compared to G6PD^{WT}. Kotaka et al. reported the structures of the N-terminal tail truncated G6PD^{WT} with G6P (15). In one of their structures (PDB ID: 2BHL), which was the only human G6PD structure reported in the literature with visible electron density for G6P, the structural NADP$^+$ was missing (a quite low occupancy), and its C-terminal tail was disordered, which were consistent with our data. The authors of 2BHL mentioned that electron density for the structural NADP$^+$ was partially observed, which indicated the affinity of NADP$^+$ in the structural NADP$^+$-binding site might be weakened in the G6P-bound state. Further analyses of the dynamics of substrate exchange, catalysis, and oligomerization would shed light on this possibly more "catalytic" role of the structural NADP$^+$.

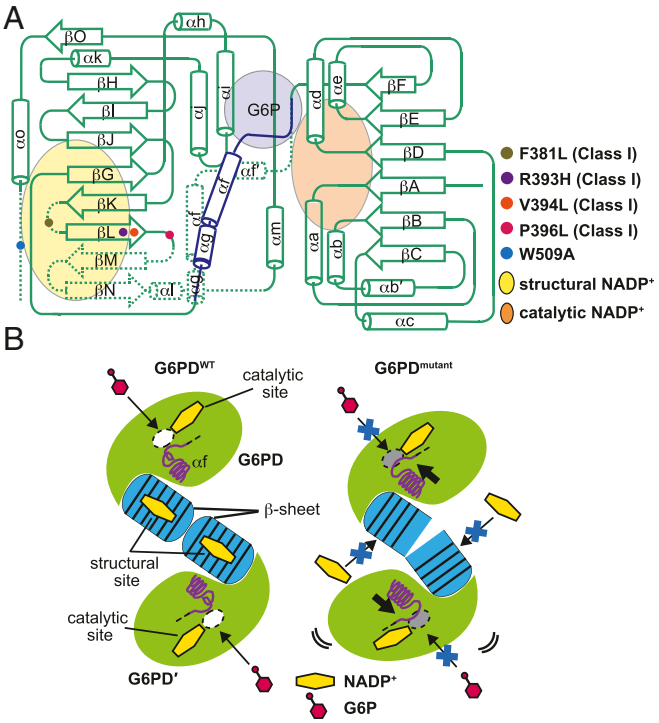

Fig. 5. Summary of structural changes caused by the class I pathogenic mutations associated with the structural NADP$^+$ binding. (*A*) Comparison of the arrangements of secondary structure elements of G6PD monomer between the wild type and the mutants. Binding sites of the catalytic NADP$^+$, structural NADP$^+$, and G6P are shown in orange, yellow, and purple, respectively. The shifted αg, αf, and stretched αf′ helices in G6PD^{mutant} are shown in blue. Disordered regions in G6PD^{mutant} are indicated by dotted lines. (*B*) Schematic representations of the G6PD^{WT} dimer (*Left*) and the G6PD^{mutant} dimer (*Right*). White and gray ovals indicate the open and occluded G6P-binding sites, respectively. Yellow hexagon indicates NADP$^+$ and its binding sites. Blue barrels at the center indicate the β-sheets that the structural NADP$^+$ molecules are bound to in G6PD^{WT} but not in G6PD^{mutant}.

The distribution of G6PD deficiency is geographically correlated with malaria prevalence, and this deficiency may protect against malaria (5, 37). Unfortunately, primaquine, which is one of the most effective drugs for malaria, *Plasmodium vivax*, causes acute hemolytic anemia in G6PD-deficient patients, probably due to malaria-induced generation of the reactive oxygen species, which cannot be efficiently reduced in patients with G6PD deficiency (38–44). To treat G6PD-deficient patients infected with malaria or having other oxidative stress-related diseases, enzymatic activity of these patients has to be improved. Our structures of the four class I G6PD mutants suggest a universal mechanism of the loss of G6PD activity in these patients. These mutations cause the loss of the structural NADP$^+$, the disorder in the C-terminal tail, shifting the αf and αf′ helices to occlude the G6P-binding site, thus leading to deficient enzymatic activity. These structural differences from the wild-type enzyme are shared by the class I mutants, whose mutations are centered around the structural NADP$^+$ and the dimer interface. The consistent set of structural information revealed in this study suggests that promising drugs against these class I mutations can be developed from compounds or peptides correcting the shift of the αf and αf′ helices or stabilizing the C-terminal tail.

Materials and Methods

Purification of Wild-Type and Mutants of G6PD. The G6PD gene was inserted into the pET28a vector. F381L, R393H, V394L, P396L, and W509A mutations were introduced by site-directed mutagenesis. N-terminal hexahistidine tag

(His-tag) fused G6PD mutants were bacterially expressed and purified using TALON superflow (Cytiva). After His-tag cleavage by the thrombin protease, G6PD was further purified using Superdex 200 HiLoad 16/600 (Cytiva) in 20 mM Tris·HCl (pH 8.0) buffer containing 150 mM sodium chloride.

Crystallization and Structure Determination of the G6PD Mutants. A total of 0.2 μL of 6 to 10 mg/mL $G6PD^{WT}$, $G6PD^{F381L}$, $G6PD^{R393H}$, $G6PD^{V394L}$, and $G6PD^{P396L}$ and 0.2 μL of crystallization solution containing 8 to14% polyethylene glycol (PEG) 4000, 100 to 200 mM magnesium chloride, 100 mM 2-(N-Morpholino)ethanesulfonic acid (MES) (pH 6.5), and 2 mM $NADP^+$ with or without 1 mM AG1 were mixed and incubated at 20 °C using the vapor diffusion method. For crystallization of $G6PD^{W509A}$, 0.2 μL of 10 mg/mL $G6PD^{W509A}$ and 0.2 μL of crystallization solution containing 10% PEG 8000, 50 mM magnesium chloride, 100 mM sodium acetate, 2 mM $NADP^+$, and 1 mM AG1 were mixed and incubated at 20 °C using the vapor diffusion method. $G6PD^{WT}$ and $G6PD^{W509A}$ were crystallized only in the condition containing AG1. A total of 30% ethylene glycol was used as a cryoprotectant. Datasets for $G6PD^{F381L}$, $G6PD^{R393H}$, $G6PD^{V394L}$, and $G6PD^{P396L}$ were collected in the condition without AG1. Crystals of the G6PD mutants formed within a week. Crystals were flash cooled with liquid nitrogen, and X-ray diffraction datasets were collected at the Beamline 12-2 in the Stanford Synchrotron Radiation Lightsource (SSRL) and the Beamline 5.0.2 in Advanced Light Source (ALS), and the Beamline 23-ID-B in Advanced Photon Source (APS). Datasets were processed by the XDS and CCP4 suites (45–47), and initial model structures were obtained by molecular replacement using *Phaser* with the truncated $G6PD^{WT}$ structure (PDB ID: 6A08) as a search model (21, 48). Refinement and model building were performed using *PHENIX* and *Coot* (49, 50). Especially for the low-resolution datasets of $G6PD^{F381L}$ and $G6PD^{R393H}$, iterative rounds of refinement with XYZ coordinates, real-space, rigid body, individual B factors, occupancies, X-ray/stereochemistry weight optimization, X-ray/atomic displacement parameters (ADP) weight optimization, and secondary structure restraints were performed using *PHENIX*. Model building of ambiguous sidechains of $G6PD^{F381L}$ and $G6PD^{R393H}$ was guided by high-resolution structures of G6PD. The final structures were validated using Molprobity (51). In the $G6PD^{P396L}$ crystal structure, the asymmetric unit contains one $G6PD^{P396L}$ molecule. $G6PD^{P396L}$ dimer was obtained by applying the crystallographic twofold symmetry operation (Fig. 1*A*), which results in a structure consistent with cryo-EM and SAXS data (Figs. 1*G* and 2, and *SI Appendix*, Fig. S4). Data processing for the G6PD wild type is described in *SI Appendix, Supplementary Methods*.

Kinetic Analysis. Enzyme activity was measured following the WHO protocol (10), using 0.05 μg of recombinant enzymes. Steady-state kinetic parameters were obtained by varying G6P (Chem-Impex International Inc) concentrations (0 to 1 mM) with a constant concentration of $NADP^+$ (Sigma) at 200 μM and similarly for $NADP^+$ (0 to 500 μM) with a constant concentration of G6P at 600 μM. Data analysis was performed using GraphPad Prism software v0.8 (GraphPad Software). The parameters were obtained by fitting the data to the Michaelis–Menten equation. All the assays were performed at 25 °C and run for 5 min. The assay was repeated in three to four independent measurements.

SAXS. SEC-SAXS experiments were performed at SSRL beamline 4-2 as the previous report with some modifications (52, 53). Experimental and analytical details are summarized in *SI Appendix*, Table S2. Briefly, $G6PD^{WT}$ and $G6PD^{P396L}$ were purified using Superdex 200 HiLoad 16/600 (Cytiva) in 20 mM Tris·HCl (pH8.0) buffer, containing 150 mM sodium chloride. A total of 5 mg/mL $G6PD^{P396L}$ and 0.2 to 30 mg/mL $G6PD^{WT}$ were prepared. For the $G6PD^{WT}$ dimer, 1 mM G6P was added to 5 mg/mL $G6PD^{WT}$. Concentrations of peak fractions corresponding to the $G6PD^{P396L}$ dimer, $G6PD^{WT}$ dimer, and $G6PD^{WT}$ tetramer were approximately estimated at 2.9, 2.6, and 2.6 mg/mL, respectively (*SI Appendix*, Fig. S2*E*). SEC-SAXS data were collected using Superdex 200 Increase PC 3.2/300 column (Cytiva). A total of 500 images were collected with 1-s exposure every 5 s at a 0.05 mL/min flow rate. After the 100th image (blank data collections), the X-ray shutter was closed until just before G6PD was eluted to keep the sample cell clean. Furthermore, an additional sample cell wash was executed during the closure. Data reduction and initial analyses were performed using the BL4-2 automated SEC-SAXS data processing and analysis pipelines, *SECPipe* (for SEC-SAXS data) and *SAXSPipe* (https://www-ssrl.slac.stanford.edu/smb-saxs/content/documentation-software-secpipe). It implements the program *SASTOOL* (https://www-ssrl.slac.stanford.edu/smb-saxs/content/documentation/sastool) and *ATSAS AUTORG* (54). The data were presented as I(q) versus q, where $q = 4\pi\sin(\theta)/\lambda$, 2θ is the scattering angle, and λ is the wavelength of the X-ray. After careful manual inspection, a total of five images (for $G6PD^{P396L}$ or $G6PD^{WT}$, respectively) were selected to generate the averaged profile for further analysis. The program *GNOM* was used for the indirect Fourier transform to estimate the distance distribution function P(r) (55). The theoretical scattering profile of the crystal structure was computed and fitted with experimental data using the program *CRYSOL* (56). The SAXS modeling program *CORAL* was employed for reconstructing disorder regions of the $G6PD^{P396L}$ crystal structure and the N-terminal disordered tail of the $G6PD^{WT}$ crystal structure (30). The structure of the βM-βN in the $G6PD^{WT}$ crystal structure was used for a rigid body to be moved during the modeling of $G6PD^{P396L}$. The M1-H27, V394-E398, Y424-D435, and C-terminal tail regions of $G6PD^{P396L}$ and the M1-H27 region of $G6PD^{WT}$ were assigned as flexible loops to be reconstructed. All other regions, including the dimer or tetramer interface, were fixed during the modeling. Twenty independent runs were performed with *P2* (for dimer) or P22 (for tetramer) symmetry. The model with the lowest k2 value was selected as the best model. All models of $G6PD^{P396L}$ showed that the disordered βM and βN strands were virtually located at the same position, closed to the catalytic site (*SI Appendix*, Fig. S4). The model with the lowest χ^2 values ($\chi^2 = 0.23$) was selected as the best model. The theoretical scattering profile of the initial CORAL model for $G6PD^{P396L}$ was computed and fitted with experimental data using the program CRYSOL (56).

Cryo-EM Single Particle Structural Analysis of G6PD Wild Type and P396 Mutant. A total of 3 μL of the purified $G6PD^{WT}$ and $G6PD^{P396L}$ was applied to the Quantifoil holey carbon grids (R1.2/1.3 Au 200 mesh) immediately after mixing with n-dodecyl β-D-maltopyranoside (Anatrace) (final concentration: 0.005%). The grids were blotted at 21 °C for 5 s and flash frozen in liquid ethane using the Leica EM GP (Leica Microsystems). Micrographs were collected using a K3 camera (Gatan) with the SerialEM software on the Titan Krios microscope (Thermo Fisher). Dose-weighted 4,255 and 4,395 movies were aligned by MOTIONCOR2, and following image processing was done using Relion 3.0.6 (57, 58) (*SI Appendix*, Fig. S3 *A* and *C*). Final resolutions were 8.4 Å and 9.5 Å with 196,579 and 48,783 particles, respectively (*SI Appendix*, Fig. S3 *B* and *D*). Crystal structures of $G6PD^{WT}$ and $G6PD^{P396L}$ were superimposed with the electron potential map of $G6PD^{P396L}$ using ChimeraX (59).

Molecular Dynamics Simulations of G6PD with and without Structural $NADP^+$. Based on the $G6PD^{WT}$ crystal structure (PDB ID: 6E08) protein dimers and tetramers were formed by a crystallographic symmetry operation deleting water molecules that led to steric clashes at their interface. The dimer system was simulated in a cubic box, while the tetramer used a dodecahedron box with a 1-nm distance to the box edge. After adding water molecules and ions to reach 154 mM NaCl concentration, the two systems consisted of approximately 317,000 atoms. Their interactions were described with the CHARMM36m forcefield for the protein, the Tip3P water model specific for the CHARMM force field, and the parameters for $NADP^+$ were created using CGenFF (60). We first minimized the whole system to eliminate steric clashes and then equilibrated in the canonical ensemble (NVT) ensemble with the v-rescale thermostat at 298 K and in the isothermal-isobaric ensemble (NPT) ensemble applying the Berendsen barostat to 1 bar for 1 ns each. The Particle Mesh Ewald (PME) method accounted for long-range electrostatic interactions with a cutoff of 1.2 nm and the cutoff for van der Waals interactions of 1.2 nm with a 2-fs time step. For the apo dimer and tetramer simulations, we eliminated all $NADP^+$ molecules from the initial structure following the same initial equilibration procedure. Mutant structures (P396L, F381L, V394L, and R393H) were created based on the X-ray structure (PDB ID: 6E08), replacing the atoms using Pymol. All molecular systems (apo/holo dimer and tetramer) were simulated for 500 to 1,000 ns. For the apo/holo dimer simulations of the wild type and carboxyl-terminal truncated P396L mutant, the results are based on five to six independent simulations, and for all the other systems, at least three replicates were simulated. The $NADP^+$-bound systems resulted in constant rmsd of the backbone atoms after 200 ns (*SI Appendix*, Fig. S5). MD simulations were carried out with the GROMACS 2019.4 package (61). Loss of secondary structure of the βM-βN strands was monitored with the dssp tool in GROMACS where the rupture was defined by a maintained drop of β-sheet content in the amino acids 397 to 428 of one monomer chain by more than 10% during the total simulation time of 500 to 1,000 ns.

Thermal Shift Assay. A total of 5 μM of $G6PD^{WT}$, $G6PD^{F381L}$, $G6PD^{R393H}$, $G6PD^{V394L}$, $G6PD^{P396L}$, and $G6PD^{W509A}$ was mixed with 5× SYPRO Orange dye (Sigma Aldrich) in the presence or absence of 10 μM $NADP^+$ (Sigma Aldrich) in 20 mM Tris·HCl (pH 8.0) buffer containing 150 mM sodium chloride. Fluoresce of the SYPRO Orange dye was measured by QuantStudio 5 (Thermo Fisher Scientific) with a temperature gradient from 25 °C to 75 °C in steps of 1 °C/min.

SEC Analysis. A total of 0.5 mg/mL of $G6PD^{WT}$, $G6PD^{F381L}$, $G6PD^{R393H}$, $G6PD^{V394L}$, $G6PD^{P396L}$, and $G6PD^{W509A}$ was incubated with or without 1 mM G6P for 1 h and subjected to the Superdex 200 Increase 10/300 GL (Cytiva) in 20 mM Tris·HCl (pH 8.0) buffer containing 150 mM sodium chloride. In this condition, the partial dissociation of the $G6PD^{WT}$ dimer to monomer was observed (*SI Appendix*, Fig. S2 *F* and *G*). The SEC analysis in the SEC-SAXS measurement with or without G6P was performed with 5 mg/mL G6PD wild type and P396L using Superdex 200 Increase 3.2/300 (Cytiva). In this condition, the dissociation of the $G6PD^{WT}$ tetramer to dimer was observed (*SI Appendix*, Fig. S2*E*). The dissociation from tetramer/dimer to dimer/monomer seems to be concentration dependent in a SEC column (Superdex 200 Increase 10/300 GL vs. Superdex 200 Increase 3.2/300) since the most population of 50 μL of 0.5 mg/mL $G6PD^{WT}$ forms a tetramer in the Superdex 200 Increase 3.2/300, whereas the most population of 50 μL of 0.5 mg/mL $G6PD^{WT}$ forms a dimer in the Superdex 200 Increase 10/300 GL.

Isothermal Titration Calorimetry. A total of 2 mL of 100 μM $G6PD^{WT}$ and $G6PD^{P396L}$ were titrated with 1 mM G6P in 20 mM MES (pH 6.0) buffer containing 150 mM sodium chloride using the MicroCal VP-iTC (Malvern). The background was measured with 1 mM G6P in 20 mM MES (pH 6.0) buffer containing 150 mM sodium chloride and subtracted from data for the G6PD wild type and the P396L mutant. Data were analyzed using the Origin70 software.

Data Availability. Protein structures have been deposited in the Protein Data Bank (PDB) with accession codes of 6VA7, 6VA8, 6VA9, 6VA0, and 6VAQ for $G6PD^{P396L}$, $G6PD^{F381L}$, $G6PD^{R393H}$, $G6PD^{W509A}$, and $G6PD^{V394L}$, respectively.

ACKNOWLEDGMENTS. This study was supported by NIH grant HD084422 (to D.M.-R. and S.W.). This work was also supported by the Japan Society for the Promotion of Science KAKENHI grant JP19K23713 and JP20K15741 (to N.H.). Use of the Stanford Synchrotron Radiation Lightsource (SSRL), SLAC National Accelerator Laboratory, is supported by the US Department of Energy (DOE), Office of Science, Office of Basic Energy Sciences under contract DE-AC02-76SF00515. The SSRL Structural Molecular Biology Program is supported by the DOE Office of Biological and Environmental Research, and by the NIH, National Institute of General Medical Sciences (NIGMS) (P41GM103393). The Pilatus detector at beamline 4-2 at SSRL was funded under NIH grant S10OD021512. This study was also supported by an NIH grant (U24GM129564) and the Stanford-SLAC cryo-EM center staff. The contents of this publication are solely the responsibility of the authors and do not necessarily represent the official views of NIGMS or NIH. We thank the beamline scientists for their assistance with data collection at the beamlines 12-2 and 4-2 of SSRL at SLAC National Accelerator Laboratory (Menlo Park), the beamline 502 of the Advanced Light Source (Berkeley), and the beamline 23-ID-B of the Advanced Photon Source at the Argonne National Laboratory (Lemont). C.C.-O. and E.V.-M. acknowledge funding by the Max Planck Society through a partner group and Fondecyt 1160193. C.C.-O. and E.V.-M. are grateful for financial support by Fondecyt project 1200369, Comisión Nacional de Investigación Científica y Tecnología: Programa Colaboración Internacional (CONICYT PCI) Max Planck Institute for terrestrial microbiology MPG 190003, Max Planck Partner Group, and the Southern CPU Cluster for providing computational resources. We thank Drs. K. M. Jude, J. Dou, and K. C. Garcia, (Stanford University) for the use of the VP-iTC and QuantStudio 5 instruments and for their assistance.

1. A. Minucci *et al*., Glucose-6-phosphate dehydrogenase (G6PD) mutations database: Review of the "old" and update of the new mutations. *Blood Cells Mol. Dis.* **48**, 154–165 (2012).
2. V. K. Bhutani *et al*., Neonatal hyperbilirubinemia and rhesus disease of the newborn: Incidence and impairment estimates for 2010 at regional and global levels. *Pediatr. Res.* **74** (suppl. 1), 86–100 (2013).
3. L. Luzzatto, C. Nannelli, R. Notaro, Glucose-6-phosphate dehydrogenase deficiency. *Hematol. Oncol. Clin. North Am.* **30**, 373–393 (2016).
4. A. D. Cunningham, S. Hwang, D. Mochly-Rosen, Glucose-6-phosphate dehydrogenase deficiency and the need for a novel treatment to prevent kernicterus. *Clin. Perinatol.* **43**, 341–354 (2016).
5. E. T. Nkhoma, C. Poole, V. Vannappagari, S. A. Hall, E. Beutler, The global prevalence of glucose-6-phosphate dehydrogenase deficiency: A systematic review and meta-analysis. *Blood Cells Mol. Dis.* **42**, 267–278 (2009).
6. J. M. Berg, J. L. Tymoczko, L. Stryer, *Biochemistry* (W. H. Freeman and Co, New York, ed. 5, 2002).
7. B. Halliwell, L. M. C. Gutteridge, *Free Radicals in Biology and Medicine* (Oxford University Press, ed. 5, 2015).
8. E. Beutler, Glucose-6-phosphate dehydrogenase deficiency: A historical perspective. *Blood* **111**, 16–24 (2008).
9. M. D. Cappellini, G. Fiorelli, Glucose-6-phosphate dehydrogenase deficiency. *Lancet* **371**, 64–74 (2008).
10. WHO Working Group, Glucose-6-phosphate dehydrogenase deficiency. *Bull. World Health Organ.* **67**, 601–611 (1989).
11. E. Beutler, G6PD: Population genetics and clinical manifestations. *Blood Rev.* **10**, 45–52 (1996).
12. L. Luzzatto, Glucose 6-phosphate dehydrogenase deficiency: From genotype to phenotype. *Haematologica* **91**, 1303–1306 (2006).
13. S. Gómez-Manzo *et al*., Glucose-6-phosphate dehydrogenase: Update and analysis of new mutations around the World. *Int. J. Mol. Sci.* **17**, 2069 (2016).
14. S. W. N. Au, S. Gover, V. M. S. Lam, M. J. Adams, Human glucose-6-phosphate dehydrogenase: The crystal structure reveals a structural NADP(+) molecule and provides insights into enzyme deficiency. *Structure* **8**, 293–303 (2000).
15. M. Kotaka *et al*., Structural studies of glucose-6-phosphate and NADP+ binding to human glucose-6-phosphate dehydrogenase. *Acta Crystallogr. D Biol. Crystallogr.* **61**, 495–504 (2005).
16. A. Bonsignore, R. Cancedda, I. Lorenzoni, M. E. Cosulich, A. De Flora, Human erythrocyte glucose 6-phosphate dehydrogenase. Physical properties. *Biochem. Biophys. Res. Commun.* **43**, 94–101 (1971).
17. N. G. Wrigley, J. V. Heather, A. Bonsignore, A. De Flora, Human erythrocyte glucose 6-phosphate dehydrogenase: Electron microscope studies on structure and interconversion of tetramers, dimers and monomers. *J. Mol. Biol.* **68**, 483–499 (1972).
18. R. Cancedda, G. Ogunmola, L. Luzzatto, Genetic variants of human erythrocyte glucose-6-phosphate dehydrogenase. Discrete conformational states stabilized by NADP + and NADPH. *Eur. J. Biochem.* **34**, 199–204 (1973).
19. X. T. Wang, T. F. Chan, V. M. S. Lam, P. C. Engel, What is the role of the second "structural" NADP+-binding site in human glucose 6-phosphate dehydrogenase? *Protein Sci.* **17**, 1403–1411 (2008).
20. A. D. Cunningham, D. Mochly-Rosen, Structural analysis of clinically relevant pathogenic G6PD variants reveals the importance of tetramerization for G6PD activity. *Matters (Zur.)* **2017**, (2017).
21. S. Hwang *et al*., Correcting glucose-6-phosphate dehydrogenase deficiency with a small-molecule activator. *Nat. Commun.* **9**, 4045 (2018).
22. A. G. Raub *et al*., Small-molecule activators of glucose-6-phosphate dehydrogenase (G6PD) bridging the dimer interface. *ChemMedChem* **14**, 1321–1324 (2019).
23. X. T. Wang, P. C. Engel, Clinical mutants of human glucose 6-phosphate dehydrogenase: Impairment of NADP(+) binding affects both folding and stability. *Biochim. Biophys. Acta* **1792**, 804–809 (2009).
24. S. Gómez-Manzo *et al*., The stability of G6PD is affected by mutations with different clinical phenotypes. *Int. J. Mol. Sci.* **15**, 21179–21201 (2014).
25. S. Gómez-Manzo *et al*., Mutations of glucose-6-phosphate dehydrogenase durham, Santa-Maria and A+ variants are associated with loss functional and structural stability of the protein. *Int. J. Mol. Sci.* **16**, 28657–28668 (2015).
26. A. D. Cunningham, A. Colavin, K. C. Huang, D. Mochly-Rosen, Coupling between protein stability and catalytic activity determines pathogenicity of G6PD variants. *Cell Rep.* **18**, 2592–2599 (2017).
27. M.-A. Jang *et al*., A novel de novo mutation in the G6PD gene in a Korean boy with glucose-6-phosphate dehydrogenase deficiency: Case report. *Ann. Clin. Lab. Sci.* **45**, 446–448 (2015).
28. S. Filosa *et al*., A novel single-base mutation in the glucose 6-phosphate dehydrogenase gene is associated with chronic non-spherocytic haemolytic anaemia. *Hum. Genet.* **94**, 560–562 (1994).
29. C. D. Putnam, M. Hammel, G. L. Hura, J. A. Tainer, X-ray solution scattering (SAXS) combined with crystallography and computation: Defining accurate macromolecular structures, conformations and assemblies in solution. *Q. Rev. Biophys.* **40**, 191–285 (2007).
30. M. V. Petoukhov *et al*., New developments in the *ATSAS* program package for small-angle scattering data analysis. *J. Appl. Cryst.* **45**, 342–350 (2012).
31. E. Beutler, B. Westwood, A. Melemed, P. Dal Borgo, D. Margolis, Three new exon 10 glucose-6-phosphate dehydrogenase mutations. *Blood Cells Mol. Dis.* **21**, 64–72 (1995).
32. Y. Okano *et al*., Two novel glucose-6-phosphate dehydrogenase variants found in newborn mass-screening for galactosaemia. *Eur. J. Pediatr.* **160**, 105–108 (2001).
33. W. Xu *et al*., Glucose-6 phosphate dehydrogenase mutations and haplotypes in various ethnic groups. *Blood* **85**, 257–263 (1995).
34. E. Beutler, W. Kuhl, T. Gelbart, L. Forman, DNA sequence abnormalities of human glucose-6-phosphate dehydrogenase variants. *J. Biol. Chem.* **266**, 4145–4150 (1991).
35. S. Filosa *et al*., Molecular basis of chronic non-spherocytic haemolytic anaemia: A new G6PD variant (393 Arg—His) with abnormal KmG6P and marked in vivo instability. *Br. J. Haematol.* **80**, 111–116 (1992).
36. M. Maciag *et al*., Molecular analysis of three novel G6PD variants: G6PD Pedoplis-Ckaro, G6PD piotrkow and G6PD Krakow. *Acta Biochim. Pol.* **54**, 877–881 (2007).
37. T. Vulliamy, P. Mason, L. Luzzatto, The molecular basis of glucose-6-phosphate dehydrogenase deficiency. *Trends Genet.* **8**, 138–143 (1992).
38. K. A. Fletcher, P. F. Barton, J. A. Kelly, Studies on the mechanisms of oxidation in the erythrocyte by metabolites of primaquine. *Biochem. Pharmacol.* **37**, 2683–2690 (1988).
39. J. Vásquez-Vivar, O. Augusto, Hydroxylated metabolites of the antimalarial drug primaquine. Oxidation and redox cycling. *J. Biol. Chem.* **267**, 6848–6854 (1992).
40. G. C. Mills, H. P. Randall, Hemoglobin catabolism. II. The protection of hemoglobin from oxidative breakdown in the intact erythrocyte. *J. Biol. Chem.* **232**, 589–598 (1958).
41. G. Cohen, P. Hochstein, Generation of hydrogen peroxide in erythrocytes by hemolytic agents. *Biochemistry* **3**, 895–900 (1964).
42. B. Goldberg, A. Stern, Superoxide anion as a mediator of drug-induced oxidative hemolysis. *J. Biol. Chem.* **251**, 6468–6470 (1976).

43. B. Goldberg, A. Stern, The generation of O2-by the interaction of the hemolytic agent, phenylhydrazine, with human hemoglobin. *J. Biol. Chem.* **250**, 2401–2403 (1975).
44. M. Summerfield, G. R. Tudhope, Studies with primaquine in vitro: Superoxide radical formation and oxidation of haemoglobin. *Br. J. Clin. Pharmacol.* **6**, 319–323 (1978).
45. M. D. Winn *et al*., Overview of the CCP4 suite and current developments. *Acta Crystallogr. D Biol. Crystallogr.* **67**, 235–242 (2011).
46. W. Kabsch, XDS. *Acta Crystallogr. D Biol. Crystallogr.* **66**, 125–132 (2010).
47. P. A. Karplus, K. Diederichs, Assessing and maximizing data quality in macromolecular crystallography. *Curr. Opin. Struct. Biol.* **34**, 60–68 (2015).
48. A. J. McCoy *et al*., Phaser crystallographic software. *J. Appl. Cryst.* **40**, 658–674 (2007).
49. P. D. Adams *et al*., Phenix: A comprehensive python-based system for macromolecular structure solution. *Acta Crystallogr. D Biol. Crystallogr.* **66**, 213–221 (2010).
50. P. Emsley, B. Lohkamp, W. G. Scott, K. Cowtan, Features and development of Coot. *Acta Crystallogr. D Biol. Crystallogr.* **66**, 486–501 (2010).
51. V. B. Chen *et al*., MolProbity: All-atom structure validation for macromolecular crystallography. *Acta Crystallogr. D Biol. Crystallogr.* **66**, 12–21 (2010).
52. M. Bush *et al*., An ensemble of flexible conformations underlies mechanotransduction by the cadherin-catenin adhesion complex. *Proc. Natl. Acad. Sci. U.S.A.* **116**, 21545–21555 (2019).
53. X. Li *et al*., Structure-function analysis of the extended conformation of a polyketide synthase module. *J. Am. Chem. Soc.* **140**, 6518–6521 (2018).
54. M. V. Petoukhov, P. V. Konarev, G. Kikhney, I. Dmitri, ATSAS 2.1–Supported small-angle scattering data analysis. *Appl. Crystallogr.* **40**, s223–s228 (2007).
55. D. I. Svergun, Determination of the regularization parameter in indirect-transform methods using perceptual criteria. *J. Appl. Cryst.* **25**, 495–503 (1992).
56. D. Svergun, C. Barberato, M. H. Koch, CRYSOL–A program to evaluate X-ray solution scattering of biological macromolecules from atomic coordinates. *J. Appl. Cryst.* **28**, 768–773 (1995).
57. S. Q. Zheng *et al*., MotionCor2: Anisotropic correction of beam-induced motion for improved cryo-electron microscopy. *Nat. Methods* **14**, 331–332 (2017).
58. S. H. W. Scheres, Processing of structurally heterogeneous cryo-EM data in RELION. *Methods Enzymol.* **579**, 125–157 (2016).
59. T. D. Goddard *et al*., UCSF ChimeraX: Meeting modern challenges in visualization and analysis. *Protein Sci.* **27**, 14–25 (2018).
60. J. Huang *et al*., CHARMM36m: An improved force field for folded and intrinsically disordered proteins. *Nat. Methods* **14**, 71–73 (2017).
61. M. J. Abraham *et al*., GROMACS: High performance molecular simulations through multi-level parallelism from laptops to supercomputers. *SoftwareX* **1–2**, 19–25 (2015).